Glubam roof truss with riveted glubam connections adopting thin-walled steel tube: Experiment, modeling, and model-updating

Journal of Building Engineering

Glubam roof truss with riveted glubam connections adopting thin-walled steel tube: Experiment, modeling, and model-updating

--Manuscript Draft--

Manuscript Number:	JBE-D-24-05483R1
Article Type:	Research Paper
Section/Category:	Sustainable construction materials
Keywords:	Glubam riveted connections; Thin-walled steel tube; Model updating; Parallel genetic algorithm; Neural network and prior knowledge
Corresponding Author:	Yongjia Xu, Ph.D. University of Illinois Urbana-Champaign CHINA
First Author:	Da Shi, PhD Candidate
Order of Authors:	Da Shi, PhD Candidate
	Yongjia Xu, Dr.
	Guoshan Lu, Dr.
	Zhi Li, Dr.
	Cristoforo Demartino, Dr.
Abstract:	Bio-based laminated structures offer a timely solution to meet the pressing demand for resource-efficient and environmentally responsible construction practices in civil engineering. Riveted connections are a kind of commonly used joint and significantly impact the mechanical behaviors of global structure. However, existing studies on the complex behavior of such joints for bamboo-based structures are insufficient. This study investigated the hysteretic behavior of riveted Glued Laminated Bamboo (glubam) connections using thin-walled steel tube and corresponding planar roof truss with thin-walled steel tube connections by experimental and numerical methods. Firstly, cyclic tests were conducted on the riveted glubam connections with thin-walled steel tube to investigate their hysteretic behavior. The test matrix encompasses four distinct connection configurations, carefully selected to assess the connection behavior of glubam. After the investigation of connection behavior, cyclic tests were further conducted on glubam planar roof truss structures to evaluate their global and local hysteretic behavior. Subsequently, the numerical hysteretic models for joints and hybrid roof trusses were developed within the OpenSeesPy framework. To accurately and efficiently calibrate the model parameters, a novel parallel genetic algorithm (PGA) was proposed to carry out an initial calibration on model parameters. Based on PGA, a more comprehensive model updating framework combining the neural network, prior knowledge and PGA was developed to obtain optimal parameters. Finally, the numerical models were successfully validated against the experimental data, demonstrating the effectiveness of the established numerical model and model-updating framework.
Suggested Reviewers:	Xinzheng Lu, Dr. Professor, Tsinghua University luxz@tsinghua.edu.cn Professor Lu is a famous professor in the field of civil engineering. He has published many papers related to sturctural response simulation and machine learning. Machine learning and structural response simulation is exactly an important part of this current study.
	Yan Xiao, Dr. Professor, Zhejiang University yanxiao@intl.zju.edu.cn Professor Xiao is a famous professor in the field of civil engineering. He has published many papers related to wood and bamboo structures. The target of this study is wood and timber structures.

Opposed Reviewers:	
Response to Reviewers:	Please see the attachment.

Cover Letter

Assistant Professor Yongjia Xu
Zhejiang University - University of Illinois at Urbana Champaign Institute, Haining 314400, Zhejiang, PR China
Email xuyongjia0904@163.com

Dear Editor,

On behalf of my co-authors, we thank you very much for giving us the opportunity to revise our manuscript. We thank the Editor and the Reviewers for their comments and suggestions concerning our manuscript.

The following responses have been prepared to address the technical comments raised by the Reviewers. Each point has been addressed in detail. In addition, we have made further revisions to the manuscript to clarify any remaining concerns. These changes have not affected the content or framework of our paper. Moreover, evident improvements of the figures and editorial quality was done to meet the high requirements of this journal.

Once again, thank you very much for your comments and suggestions!

On behalf of the authors,

Yongjia Xu,

Assistant Professor
Zhejiang University / University of Illinois at Urbana Champaign Institute (ZJUI),
Email: xuyongjia0904@163.com

Declaration of interests

☒The authors declare that they have no known competing financial interests or personal relationships that could have appeared to influence the work reported in this paper.

☐The authors declare the following financial interests/personal relationships which may be considered as potential competing interests:

Da Shi: Methodology, Software, Formal analysis, Writing - Original Draft, Validation

Yongjia Xu: Methodology, Software, Formal analysis, Writing - Review & Editing

Cristoforo Demartino: Conceptualization, Supervision, Funding acquisition

Guoshan Lu: Investigation, Resources, Writing - Review & Editing

Zhi Li: Methodology, Writing - Review & Editing

Glubam roof truss with riveted glubam connections adopting thin-walled steel tube: Experiment, modeling, and model-updating

Da Shi[a,b], Yongjia Xu[c,d,*], Cristoforo Demartino[c,d], Guoshan Lu[e], Zhi Li[a]

[a] *College of Civil Engineering and Architecture, Zhejiang University, 866 Yuhangtang Road, Hangzhou, 310058 Zhejiang, PR China*

[b] *Politecnico di Torino, DISEG, Dipartimento di Ingegneria Strutturale, Edile e Geotecnica, Corso Duca Degli Abruzzi, 24, Turin, 10128, Italy*

[c] *Zhejiang University - University of Illinois, Urbana Champaign Institute, Haining 314400, Zhejiang, PR China*

[d] *Department of Civil and Environmental Engineering, University of Illinois, Urbana-Champaign, Urbana, IL 61801, USA*

[e] *College of Civil Engineering, Nanjing Tech University, Nanjing 211800, China*

Abstract

Bio-based laminated structures offer a timely solution to meet the pressing demand for resource-efficient and environmentally responsible construction practices in civil engineering. Riveted connections are a kind of commonly used joint and significantly impact the mechanical behaviors of global structure. However, existing studies on the complex behavior of such joints for bamboo-based structures are insufficient. This study investigated the hysteretic behavior of riveted Glued Laminated Bamboo (glubam) connections using thin-walled steel tube and corresponding planar roof truss with thin-walled steel tube connections by experimental and numerical methods. Firstly, cyclic tests were conducted on the riveted glubam connections with thin-walled steel tube to investigate their hysteretic behavior. The test matrix encompasses four distinct connection configurations, carefully selected to assess the connection behavior of glubam. After the investigation of connection behavior, cyclic tests were further conducted on glubam planar roof truss structures to evaluate their global and local hysteretic behavior. Subsequently, the numerical hysteretic models for joints and hybrid roof trusses were developed within the OpenSeesPy framework. To accurately and efficiently calibrate the model parameters, a novel parallel genetic algorithm (PGA) was proposed to carry out an initial calibration on model parameters. Based on PGA, a more comprehensive model updating framework combining the neural network, prior knowledge and PGA was developed to obtain optimal parameters. Finally, the numerical models were successfully validated against the experimental data, demonstrating the effectiveness of the established numerical model and model-updating framework.

Keywords: Glubam riveted connections, Thin-walled steel tube, Model updating, Parallel genetic algorithm, Neural network and prior knowledge

*Corresponding author: Yongjia Xu

Email addresses: da.21@intl.zju.edu.cn (Da Shi), xuyongjia0904@163.com (Yongjia Xu), cristoforodemartino@intl.zju.edu.cn (Cristoforo Demartino), blinklu43@gmail.com (Guoshan Lu), li_zhi@zju.edu.cn (Zhi Li)

1. Introduction

Sustainable structures made from bamboo are of great importance in a rapidly evolving world, as they address the urgent requirement for more resource-efficient and environmentally responsible civil engineering construction. Bio-based laminated composite materials are widely used in construction due to their mechanical properties, economic efficiency, and potential carbon storage capacity [1, 2]. At present, glued laminated bamboo (glubam) are mainstream engineered bamboo products for structural applications [3, 4, 5, 6]. The application of glubam combined with riveted hollow joints has numerous advantages, primarily including low cost, ease of installation, and superior long-term performance. According to Sharma et al. [7], the use of bamboo in construction can reduce material costs by up to 30% compared to conventional materials. The construction process is simplified with glubam bars and riveted hollow steel tube joints. Glubam's lightweight nature facilitates easier handling and transportation, reducing labor costs and minimizing construction time. The prefabrication of glubam components allows for precise manufacturing and quick assembly on-site. Riveted hollow steel tube joints provide robust and flexible connections that can be assembled with standard tools, eliminating the need for specialized equipment. This combination enhances the overall efficiency of the construction process. Studies by Li and Li [8] demonstrate that prefabricated bamboo and steel structures can reduce construction time by up to 40%.

However, traditional glue laminated bamboo joints have high strength but low ductility [4, 9], which hinders the effort towards enhancing better seismic resilience and raising the necessities of developing ductile joints for glubam structures. Among all the potential connection types, glue-laminated bamboo (glubam) combined with riveted hollow steel tube joints has emerged as a promising solution. Rivets joints are fasteners that are not threaded and have a cylindrical rod with combined heads short in length, and are widely used in connecting individual components together in joints structure. Compared with bolted connections at comparable design loads, riveted bamboo connections exhibited excellent seismic performance, with respect to strength deterioration, deformation ability, ductility, and energy dissipation [10, 11]. Additionally, the riveted hollow steel tube joints are relatively inexpensive and require less material than solid steel connections, further contributing to cost savings [12].

Through both experimental and finite element analysis, Murty et al. explored the axial tensile behavior of a specific riveted connection, employing small-diameter tube fasteners in tight-fitting holes and steel plate elements in slots at the ends of joined members. Seismic response of braced timbers frames with riveted connections was investigated by Chen and Popovski based on pushover analysis. Popovski and Karacabeyli [10] carried out analytical studies on the seismic performance of braced timber frame buildings using riveted connections to assess the force modification factors utilizing a simplified nonlinear dynamic analysis method.

The long-term performance of structures utilizing glubam bars with riveted hollow steel tube joints is another significant aspect. Glubam exhibits a high resistance to biological degradation due to its dense

structure and natural silica content. However, it is crucial to ensure proper treatment and coating to enhance its durability. When adequately treated and coated, glubam can resist moisture absorption, which is essential in preventing rot and fungal growth. Studies have shown that water-repellent coatings and sealants significantly improve its performance in humid environments [14]. In addition, bamboo is susceptible to insect attacks and fungal growth if not properly treated. Applying borates or other preservatives can effectively protect glubam from termites and other wood-boring insects. Exposure to ultraviolet (UV) radiation can cause surface degradation in bamboo. Protective coatings, such as UV-resistant varnishes, can mitigate this effect and prolong the material's life [15]. Noting that the long-term durability is not the main focus of this study, thus will not be further discussed in the following sections.

Structural performance of bamboo and timber-based structures is usually governed by the nonlinear response in the connection zones, where high deformation levels and stress concentrations are developed around the fasteners (rivets, nails, dowels or bolts). These zones are also susceptible to significant load-reversals during the service life of structures, especially during extreme scenarios such as earthquakes or strong winds. For this reason, the nonlinear behavior of riveted glubam connections under large deformation levels until failure is worth investigating. The existing numerical simulation work on rivet connections was often conducted through 3D finite element models [16, 17, 18, 19, 20], which incurred high computational costs and were not suitable for full-scale global structure analysis. Therefore, developing a simplified phenomenological model to simulate the hysteresis behavior of rivet joints is necessary.

To simulate the complex behaviors of riveted glubam connections mentioned above, the proposed numerical model is expected to include a large number of flexible parameters. Hence, automatic parameter calibration is indispensable. In existing studies, many data-driven model updating methods are investigated, including the Newton and modified Newton method, Quasi-Newton methods, least-square regression, Bayesian optimization method, genetic algorithm (GA), particle swarm algorithm, and neural network-based methods Ehrlich [21], Dennis and More [22], Astroza et al. [23], Yu et al. [24], Ebrahimian et al. [25], Astroza et al. [26], Sessa et al. [27], Wang et al. [28], Do and Ohsaki [29], Gu et al. [30], which are proved to be effective in updating unknown parameters of different numerical models. However, for the highly non-linear and non-convex optimization problem, these updating method may result in an unacceptable computational burden or unsatisfactory performance. A highly parallel and accurate framework for parameter optimization is required.

In this study, the axial behavior of riveted glubam connections with thin-walled steel tube were investigated by experimental and numerical simulation methods. At first, axial hysteretic test was carried out on the riveted glubam connections and roof truss structures integrated with corresponding connections, and a total of four configurations of connections were considered herein (Sections 2 and 3). The experimental results are provided and analyzed in Section 4. Then, nonlinear models were proposed based on OpenSeesPy [31] and adopted to carry out the nonlinear time-history analysis on truss joints and global roof truss system

(Section 5). Finally, a more comprehensive model updating framework combining the neural network, prior knowledge and parallel genetic algorithm (PGA) was developed to obtain optimal parameters (Section 6). Finally, the numerical models are comprehensively validated against the experimental data (Section 7).

2. Roof truss: Materials, Design, and Construction

2.1. Details of joints

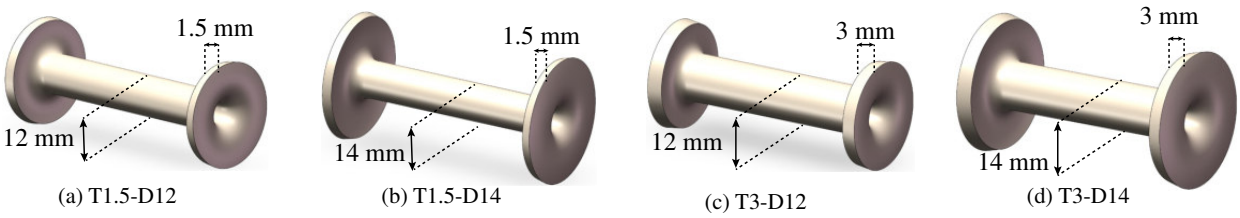

(a) T1.5-D12 (b) T1.5-D14 (c) T3-D12 (d) T3-D14

Figure 1: Sketch of steel tube with rivet head accounting for different variables

Existing research on the use of a timber truss indicates that the joint region significantly influences the overall performance of truss structures [32]. Well-designed joints can effectively improve the overall performance of truss structures [33, 34]. Therefore, four different configurations of truss joints that account for different test variables, including wall thickness of steel tube (1.5 or 3 mm) and diameter of steel tube (12 or 14 mm), as shown in Figure 1, were considered in this study. The design process was carried out following the geometric requirements of GB50005 [35]. However, considering that GB50005 [35] only provide regulations on the shape and size of bolted fasteners, and do not have relevant provisions for fasteners forms such as hollow rivets, the geometric form of the target connections is designed based on the geometric requirements for bolt connectors [35]. According to the actual application scenarios of this structural form and the size of the glubam members used, bolts with diameters of 12 mm and 14 mm should be selected. Moreover, considering the available wall thicknesses of hollow tubes of these diameters on the market and the ease of flanging the hollow tubes [36], the wall thicknesses of hollow tubes are selected as 1.5 mm and 3 mm. Details regarding the geometry of the joints are presented in Figure 2. The truss elements sandwiched within two steel plate were composed of the glubam panel, stainless steel tube, and a Q235 steel plate. Holes were drilled on glubam components and steel plates, and steel tubes fasteners were inserted in these tight-fitting holes to connect the steel plate with glubam components at the ends of joined members. In order to facilitate the smooth insertion of the hollow tube into the hole, the diameter tolerance between the hole and the hollow tube was set to 1.5 mm. This tolerance was achieved through CNC instruments.

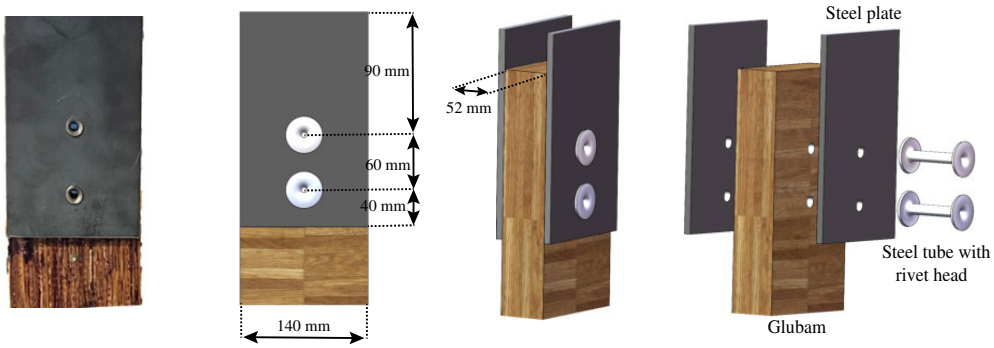

Figure 2: Detailed geometry of the riveted steel to glubam joints.

2.2. *Hybrid roof trusses*

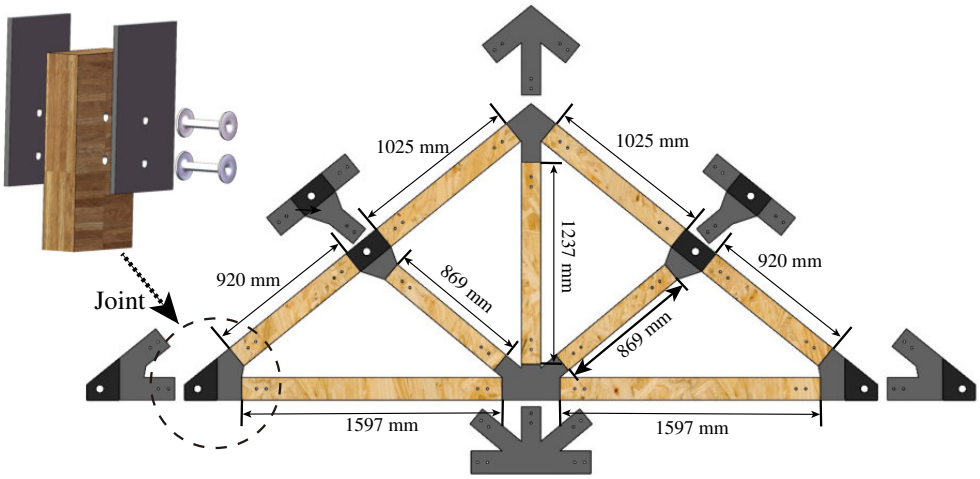

Figure 3: Detailed geometry of the roof truss.

A total of four hybrid roof trusses were specially designed and assembled, corresponding to the four different configurations of truss joints mentioned above. Each roof truss is made up of nine members and has a span of about 4.09 m. The detailed geometry of the planar truss is presented in Figure 3. All the members were connected by using steel plates and riveted glubam connections with thin-walled steel tubes. The shape of each steel plate was adapted depending on the specific number of branches at the considered node. Detailed shapes of the steel plates are also presented in Figure 3. All the truss members were automatically manufactured using a CNC drilling machine (Uli-CNC, model K1). During the manufacturing process, the glubam bars were initially cut to specified lengths. Subsequently, two holes were precisely drilled at both ends of each bar. Finally, to facilitate loading test, 50 mm diameter holes were drilled at the end steel plates of the lower chord and the middle steel plate of the upper chord to insert hinge pins. These hinge pins established connections between the truss and the hinge supports or the loading actuators, respectively.

Noting that a "strong joint, weak component" damage pattern is typically recommended in structural design to prevent the catastrophic consequences of joint failure. However, in this study, one of the primary objectives is to analyze the joint behavior, including the damage pattern and numerical model verification in deterioration stages. Therefore, the experimental design should permit joint damage to occur.

3. Test configurations

3.1. Test on truss joints

A series of axial cyclic tests on the four different joints were conducted. A sketch of the experimental setup is shown in Figure 4a. The hydraulic actuator installed vertically on the steel frame was utilized to apply the loading force through the predefined displacement. During the experiment, the actual displacement displays a difference from the predefined displacement. To solve this problem, a displacement transducer (linear variable differential transformer (LVDT)) is attached to the surface of the connections. The upper end of the displacement transducer is fixed at the end of the upper steel plate (see Figure 4) so that it moves with the actuator, and the bottom end is fixed on the middle part of glubam elements. Control of the actuator is conducted based on the slip between the upper steel plate and the glubam components, as recorded by the displacement transducer.

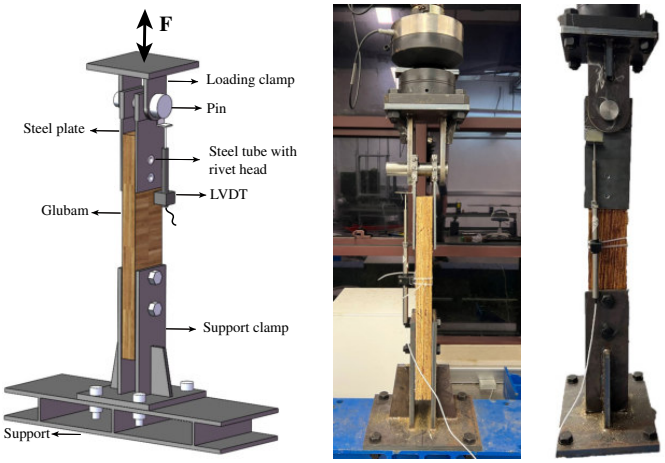

(a) (b)

Figure 4: Test setup and instruments for joints.

The cyclic loading protocol was conducted under displacement control, with a loading rate of 0.2 mm/s until failure (failure modes are discussed in the following sections) according to EN12512 [37]. The joints specimens were named following the designation A-B-RTJ, where A is wall thickness of steel tube, B is outer diameter of steel tube, and RTJ refers to the roof truss joint.

3.2. Test on the roof truss

Cyclic tests were also conducted on a series of full-scale roof trusses to obtain a hysteretic curve. The experimental setup for the planar truss is displayed in Figure 5. In this test, the end connections of the truss were joined to two steel supports attached to the foundation using hinge pins, as shown in Figure 5. Two other hinge pins were inserted into the middle steel plates that were situated between the upper chords to establish a connection with the loading instrument. A hydraulic actuator was installed vertically on a reaction frame, thus enabling the application of the target displacement time-series. Vertical force is applied to the loading beam through the hydraulic actuator, then symmetrically transmitted to the two nodes of the roof truss via loading clamps attached to the beam's left and right ends.

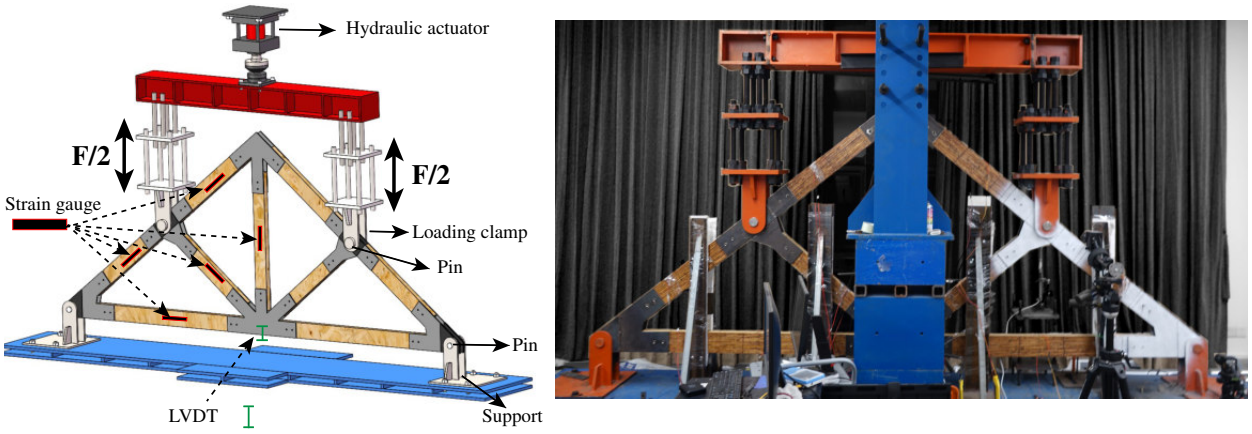

Figure 5: Test setup of glubam roof truss.

It should be noted that this study seeks to analyze the uniaxial behavior of truss structures and joints. Consequently, it is crucial to ensure that all truss elements experience only axial forces during the loading process. A lateral bracing system was applied herein to effectively constrain out-of-plane deformation, as shown in Figure 5. Several steel plates and braces were installed to prevent the deformation in the perpendicular direction. Therefore, only the constitutive law along the axial direction (parallel to the truss chord) is considered. Strain gauges were utilized to measure the strains of the truss elements accurately. The configuration of the strain gauges is depicted in Figure 5. Considering symmetry of the loads and geometry, strain gauges were only instrumented on half of the truss elements. Each truss was equipped with two strain gauges, positioned on both the top and bottom parts, to facilitate the assessment of internal moments. A LVDT is attached to the middle node between the two lower chords to detect the vertical deflection.

The cyclic loading protocol was also conducted under displacement control at a loading rate of 0.2 mm/s according to EN12512 [37]. The tested planar trusses were named following the designation A-B-RT, where A is wall thickness of steel tube, B is outer diameter of steel tube, and RT refers to roof truss.

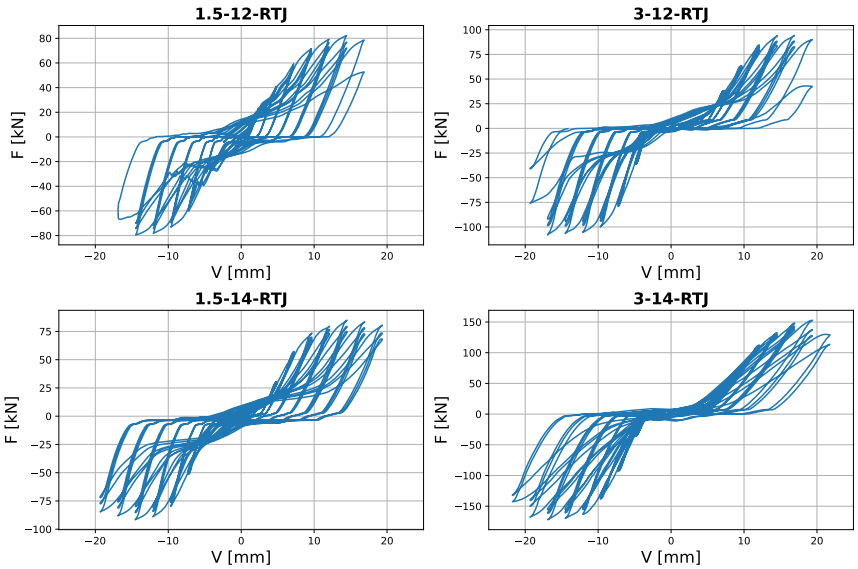

Figure 6: Load-displacement curves obtained from roof truss joint tests under cyclic loading.

4. Test results

4.1. Test results of truss joints

Figure 6 displays the hysteresis curves obtained from the cyclic loading tests conducted on the four different types of truss joints. The loading process covers the initial slip, elastic phase, yielding phase, loading plateau, and failure. The initial slip stage happened due to the tolerance between the steel tube and hole drilled on the glubam components.

Generally, the designed joints performed ductile behavior. As shown in Figure 7, joints will fail either due to the fracture of steel tube in the middle of the tube section or due to shearing fracture of riveted head. In thinner tubes, the stress is more evenly distributed across the cross-section during loading. This even distribution leads to a more uniform deformation, enhancing energy dissipation. Additionally, thinner tubes typically fail through more ductile modes such as buckling or yielding, which involve significant energy absorption. On contrast, thicker tubes may fail through more brittle modes such as cracking or localized yielding, which involve less energy absorption.

4.2. Test results of roof truss

The hysteresis curves of four groups of planar roof trusses under cyclic loading are presented in Figure 8. The planar roof truss displayed similar hysteresis responses with corresponding truss joint. However, the hysteresis curves of the planar truss exhibited a more obvious initial slip stage, especially on the compressive loading side. This could be attributed to the tolerance observed between the steel support and the hinge pin, and the slight out-of-plane movement seen under the influence of compressive loading. The typical failure

Figure 7: Failure patterns of riveted connections.

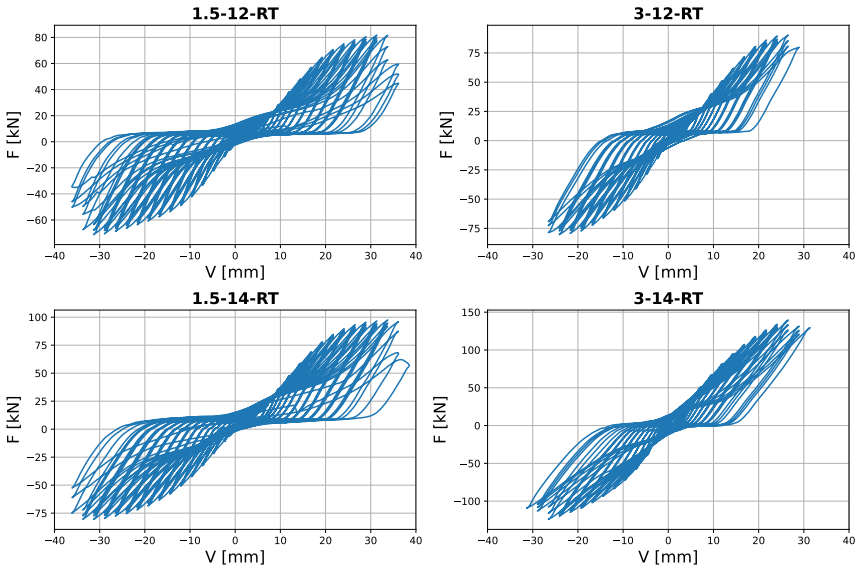

Figure 8: Load-displacement curves obtained from planar roof truss tests under cyclic loading.

patterns of the tested roof trusses are shown in Figure 9. The failures of nearly all specimens originated from the upper truss chords (the one connected with support). The two end joints of this chord either failed due to the fracture of steel tube or the shear damage of riveted head, which is similar to that in tests on single joints. This phenomenon was in good agreement with the stress status of each bar (discussed in Section 7).

Consistent with joint experiments, roof trusses with thicker steel tube joints exhibit lower energy dissipation capacity and ductility, but higher load-bearing capacity. As the diameter of the steel tube increases, the energy dissipation capacity of the roof truss improves. It can be observed that the case 3-14-RT exhibits the highest load-bearing capacity, 1.5-14-RT exhibits an optimal energy dissipation capability, while the case 3-12-RT shows the poorest performance.

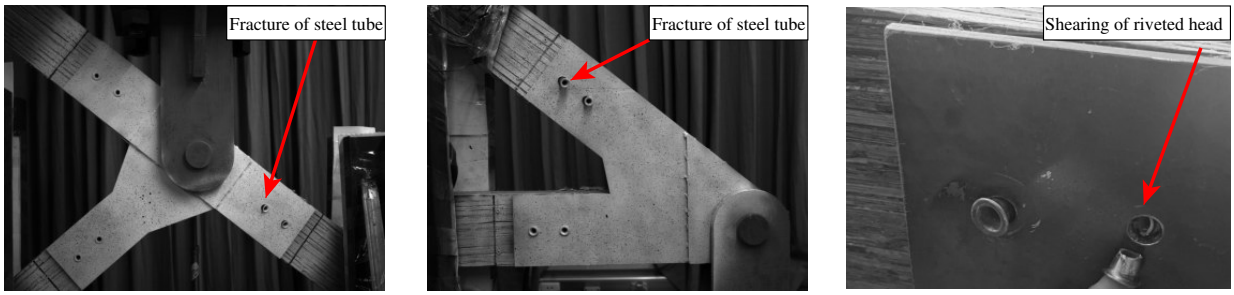

Figure 9: Typical failure pattern of planar roof trusses.

5. Numerical investigation

5.1. Hysteresis model for the truss joints

Existing phenomenological models cannot simulate the complex behaviors of the riveted glubam connections with thin-walled steel tubes, which prevents attaining a comprehensive understanding of their behaviors. To address this problem, an empirically numerical model composed of multi material models combined in series and/or parallel was developed to simulate the hysteretic behavior of a riveted connection employing the OpenSeesPy. As shown in Figure 10, the proposed model is made up of a Pinching4 spring element, two ideal elastic perfectly-plastic gap (IEPPG) uniaxial material elements and an elastic spring in series and/or parallel.

Glubam is a typical bio-based material. The hysteretic behavior of glubam connectors is similar to that of traditional timber connectors to some extent, exhibiting significant pinching effects. As an orthotropic material, its mechanical behavior varies between tensile and compressive directions, resulting in a markedly asymmetric hysteresis curve. Furthermore, glubam is prone to fracture, and its load-bearing capacity significantly decreases after fracturing. Consequently, models simulating the hysteretic behavior of glubam connectors must account for pinching, asymmetry, and fracture phenomena. The Pinching4 material is the most suitable phenomenological model for this purpose. Therefore, the Pinching4 material model utilized piece-wise linear curves to depict a pinched load-deformation response. This model, characterized by 38 parameters, accounts for cyclic stiffness and strength degradation, offering a comprehensive approach to understanding joint dynamics. Detailed descriptions of the Pinching4 parameters is provided in Table A.10 in Appendix A. The hysteresis rule for the Pinching4 element under cyclic loading is shown in Figure A.23 [38, 39].

The IEPPG material model is characterized by three properties: initial gap, elastic stiffness and yield stress, as defined in Table A.11. It exhibits zero stiffness until reaching a deformation equal to the gap length. After the gap, the IEPPG exhibits perfectly elastic behavior up to a certain point, after which it behaves as a perfectly plastic material [31]. More specifically, the tensile gap was set to Gap1 and the

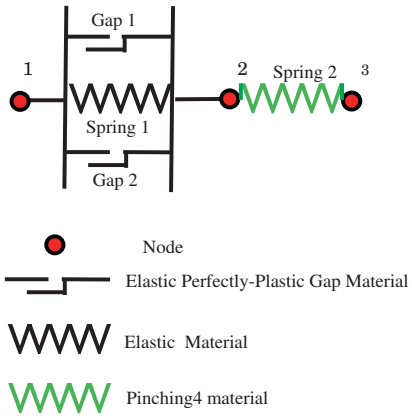

Figure 10: Proposed empirically numerical models for riveted connections.

compression gap was set to Gap2. The elastic modulus E_{gap} was set to a relatively large value so that there was no longer significant deformation after the displacement reached certain values. The purpose of setting Gap1 and Gap2 was to simulate the initial slip behavior in the positive and negative directions. The elastic stiffness of Spring 1 was set to a relatively small value (herein, 1 was adopted) to improve the analytical convergence between the initial slip segment.

Since the global non-linear behavior of the planar roof truss is highly dependent upon the joint response, the proper calibration of the single joint hysteresis model is a critical step for accurately simulating the global non-linear behavior of the planar roof truss. Globally, the proposed hysteresis model for the roof truss joints is governed by a total of 40 parameters, among which 38 are taken from Pinching4 element, and 2 from the Gap elements. To obtain a robust empirical model, it is necessary to carry out parameter identification. Considering that the proposed model features a wide array of flexible parameters, automatic parameter calibration is essential. Therefore, a novel PGA connected with OpenSeesPy was proposed in this study for automatic parameter identification, and the parameters of the aforementioned hysteresis model for the joints are preliminary calibrated based on the PGA to achieve a reasonable match with experimental results in terms of force-displacement response.

5.2. Modeling approach for the planar roof truss

Open-source and widely-recognized finite element (FE) nonlinear modeling software OpenSeesPy [31] is adopted for developing the numerical model. The proposed approach described in this study is a phenomenological macro-modeling method of the hybrid planar roof truss, as shown in Figure 11. The model is a two-dimension model with three degree-of-freedoms per node. All the rotations of the nodes were fixed since the truss elements are not accounting for rotations. The truss chords were modeled by using truss elements that include elastic uniaxial materials because we have made proper design to ensure that the

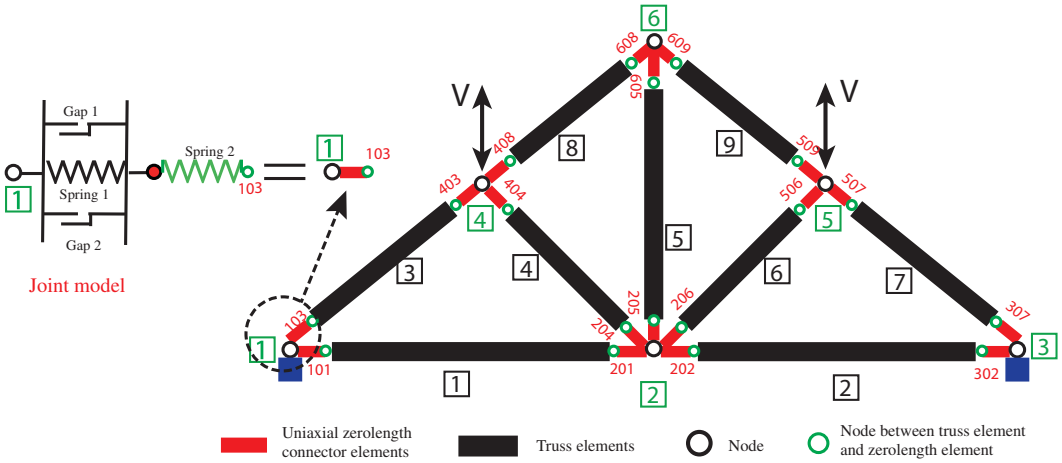

Figure 11: Simplified numerical model of the glubam roof truss with riveted joints.

damage is anticipated to occur at the joints. All of the truss chords were connected using zero-length elements. Furthermore, the truss elements and corresponding truss joints (uniaxial zero-length elements) were interconnected in series. The various branches of the steel plates were associated with distinct uniaxial zero-length connector elements, with overlapped nodes (see Figure 11). The behavior of the zero-length elements was defined in a different way in the direction parallel or perpendicular to the truss. In the perpendicular direction, an elastic material with relatively high stiffness (10^4 kN/mm) was employed to simulate rigidity of the connection consistently with experimental observations. In the parallel direction, the constitutive behavior of the uniaxial zero-length connector elements that represented the truss joints was defined by using the empirical hysteresis model discussed in the following section (see Figure 10).

The vertical load was applied as a displacement history at the two middle node between the corresponding two upper chords (nodes 4 and 5) in the OpenSeesPy model (see Figure 11). Nodes 1 and 3 were set as hinged with bearings. In this way, the boundary conditions were the same as that in the experiment.

5.3. Preliminary parameter identification of single joint model

5.3.1. PGA in parallel computing system

Genetic algorithm (GA) is widely adopted in many fields, but is often time-consuming. The most time-consuming operation within GA is the evaluation of the fitness function [40, 41]. An effective solution to this problem is taking advantage of high performance computing techniques, such as distributed or parallel computing. The idea here is to distribute workload of the algorithm among multi-threads of a single computer based on a so-called master–slave configuration, as shown in Figure B.24. By scripting programming in Python, the proposed PGA can be fully automated to interact with OpenSeesPy for generating and screening structural models as well as carrying out a multi-thread parallel numerical analysis for each parameter combination generated during the identification process. More details can be found in [42].

5.3.2. *Identification results*

Table 1: Setting of the PGA.

Population size	Number of generations	Evaluation	Number of slave threads	Number of cores per thread
60	100	6000	15	2

The model parameters were roughly determined according to our previous study [43, 6, 42], and then an amplification factor 10 and a reduction factor 0.2 for rough estimation values of all the parameters are selected as the upper bound and lower bound of the searching space. The setting of PGA was reported in Table 1. The population size and generation number are selected as 60 and 100, so the identification process will perform a total of 6000 times evaluation. 15 slave threads are arranged to evaluate 60 individuals in each generation and 2 processors are distributed to execute each thread.

Under the above settings, the identification process for the reference model has shown the convergence history illustrated in Figure 12, where the objective function evaluations represent the mean square error between the simulated response and the experimental results. In the same diagram, the moving average trend is also reported. It can be observed that the algorithm tends to a stable solution after 40-60 generations, which corresponds to 2400-3600 evaluations of individuals. The prediction results of the best individual are compared with the tested results, as shown in Figure 12. According to the results, a reasonable agreement is achieved after identification through PGA.

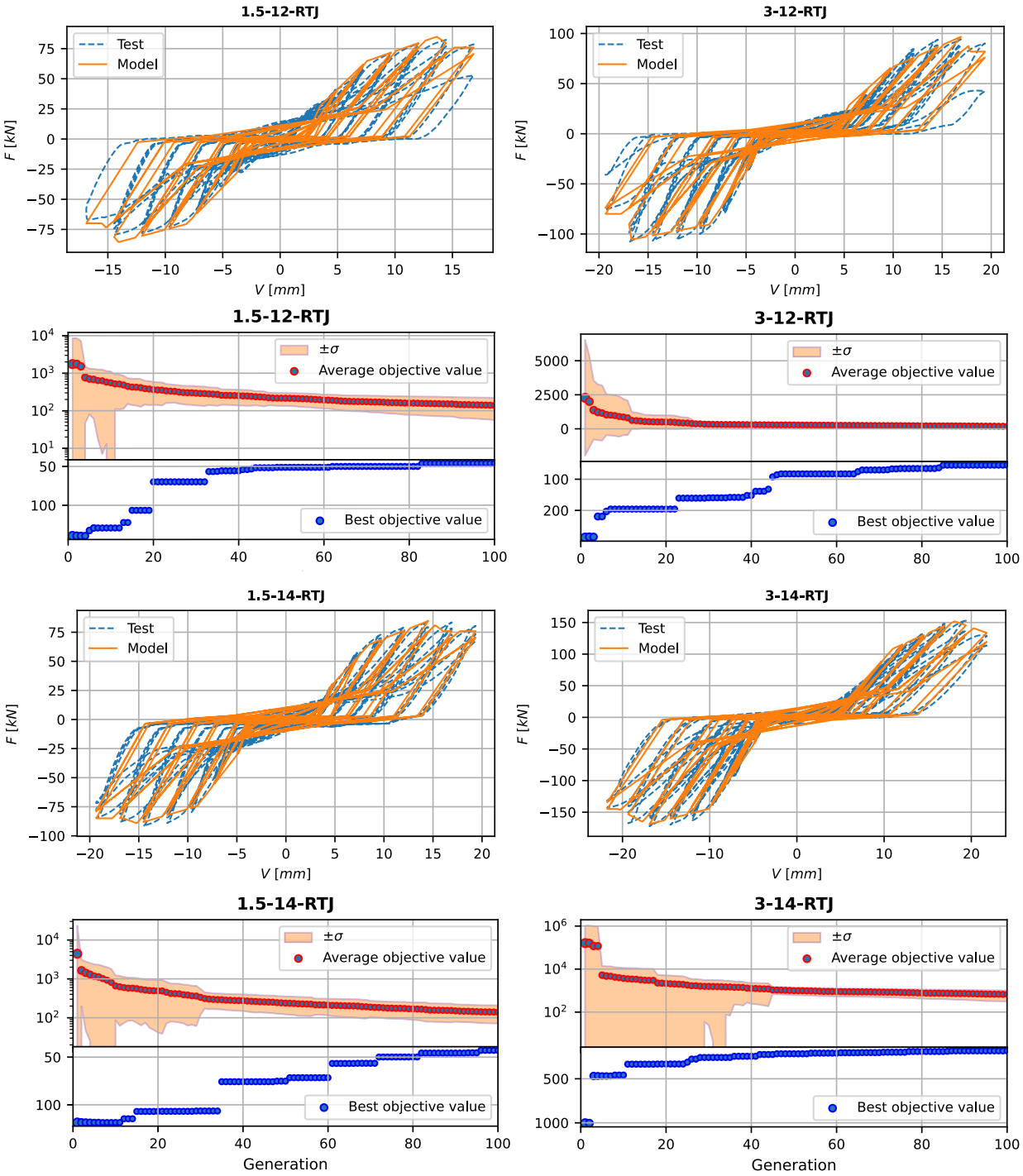

Figure 12: Comparison of tested hysteretic behavior and the best simulated hysteretic behavior, and convergence history of the identification process.

5.3.3. *Comparison of PGA settings*

Identifying appropriate parameter settings for PGA can significantly enhance optimization efficiency

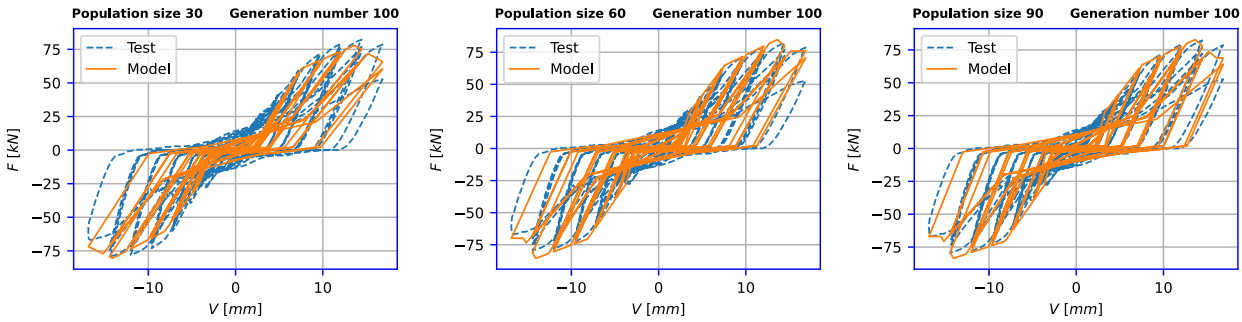

Figure 13: Comparison of identification accuracy for different population sizes.

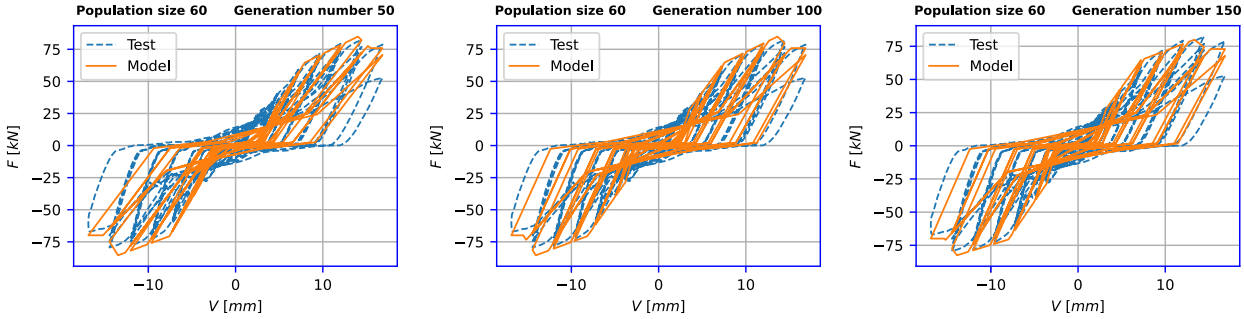

Figure 14: Comparison of identification accuracy for different generation numbers.

while maintaining accuracy. Therefore, this paper compares the optimization accuracy of PGA under various parameter settings. Population size and the number of generations are the most sensitive parameters affecting the optimization process of genetic algorithms. Therefore, we first fixed the number of generations at 100 and compared the identification accuracy for population sizes of 30, 60, and 90, as shown in Figure 13. The results indicate that when the number of generations is 100, the identification accuracy for a population size of 60 is significantly higher than for a population size of 30, while the accuracy for a population size of 90 is not much different from that of 60.

Besides, we fixed the population size at 60 to investigate the effect of the number of generations on identification accuracy. Scenarios with 50, 100, and 150 generations are examined, as shown in Figure 14. It was observed that with a population size of 60, the model prediction results significantly deviated from the experimental results when the number of generations was only 50. However, there was no significant difference in prediction accuracy between 100 and 150 generations. In summary, the settings of PGA shown in Table 1 successfully balance the accuracy and efficiency.

To quantitatively compare the identification accuracy of PGA, the prediction deviations are measured through Relative Root Mean Square Errors (RRMSE), as shown in Table 2. The RRMSE provides a

Table 2: $RRMSE$ under varying settings of PGA for the case 1.5-12-RTJ.

Setting	Generation number =100			Population size = 60		
	Population size			Generation number		
	30	60	90	50	100	150
	23.41%	11.35%	12.68%	29.35%	11.35%	8.59%

Table 3: Comparison of the traditional GA and PGA.

Method	Parallel genetic algorithm	Traditional genetic algorithm
Accuracy	$RRMSE$=11.35%	$RRMSE$=12.51%
Batch Number	400 (6000 / 15)	6000

measurement of the error between two signals, **a** (tested value) and **b** (predicted value), and is defined as:

$$RRMSE\left(\mathbf{a},\mathbf{b}\right)=\frac{\sqrt{\left[\frac{1}{N_s}\sum_{i=1}^{N_s}\left(a_i-b_i\right)^2\right]}}{\sqrt{\left[\frac{1}{N_s}\sum_{i=1}^{N_s}\left(a_i\right)^2\right]}}\times 100\left(\%\right) \tag{1}$$

where N_s denotes the total number of data samples in the signals, and i represents the number of steps in those sequences.

5.3.4. Comparison between the traditional GA and PGA

The proposed PGA was compared with the traditional GA regarding identification accuracy and efficiency, as shown in Table 3. The search space defined by the traditional GA is consistent with that of the PGA, as determined in our previous study [43, 42, 6]. From Table 3, it can be seen that the PGA and the traditional GA exhibit comparable identification accuracy. Theoretically, the PGA and GA are the same in terms of statistical accuracy. In this manuscript, the accuracy of PGA is slightly higher, which may lie in the inherent uncertainty of GA evaluation process. Meanwhile, the PGA significantly enhances identification efficiency by decreasing the number of evaluation batches.

6. Model Updating for roof truss

Although the preliminary parameter identification is carried out in Section 5.3, the stability of the heuristic algorithm is still challenging, and the identification accuracy can be further improved. Therefore, an innovative model updating method coupling the prior knowledge, neural network and PGA is proposed in this section.

6.1. Framework and methodology

The overall framework of the proposed method is shown in Figure 15. This framework consists of five key steps: (1) Latin Hypercubic Sampling (LHS) from a uniform distribution; (2) Reverse normalization based on prior knowledge; (3) Preliminary parameter identification based on neural networks; (4) PGA optimization on the joint scale; and (5) PGA optimization on the roof truss scale.

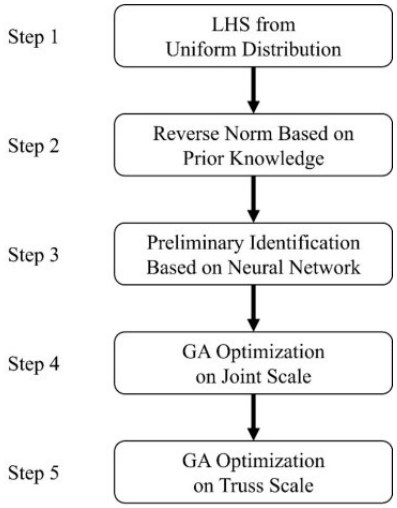

Figure 15: Framework of the proposed model updating method

6.1.1. LHS from uniform distribution

Due to the large number of flexible parameters, a complete traversal of possible parameter combinations is impossible. Therefore, to select the representative parameter combinations for the neural networks (introduced in Section 6.1.3), the LHS method [44] is adopted in this step. LHS ensures that each parameter is uniformly sampled across its entire range, thereby reducing sampling redundancy and improving the representativeness of the sample. The efficiency and effectiveness of the LHS method has been verified in many existing studies [45, 46]. Noting that, due to the existence of the reverse normalization in Step 2 (introduced in Section 6.1.2), the LHS is carried out on the uniform distribution within the range (0,1) for all parameters.

6.1.2. Reverse normalization based on prior knowledge

The original parameter sampled in Step 1 are reversely normalized back to a proper range in this step. Apparently, the parameters of the proposed numerical model cannot be randomly selected. The physical meanings of parameters, the preliminary optimization results in Section 5.3, and the experimental results are all helpful in determining the proper range of each parameter. Meanwhile, the bias-variance trade-off should also be considered in range determination, which means that a larger searching space brings a

Table 4: Parameter ranges for all flexible parameters

Parameters	Range	Motivation and description
$ePf_1, ePd_1, eNf_1, eNd_1$	(0.2, 2.0) $\rtimes$ $Para_R$	The minimum values of these parameters are generally not very close to 0.
$ePf_2, ePd_2, eNf_2, eNd_2$		
$ePf_3, ePd_3, eNf_3, eNd_3$	(0.0, 3.0) $\rtimes$ $(Para_R - Para_{RL}) + Para_{RL}$	The values of these parameters are generally larger than corresponding values describing the last key point.
ePd_4, eNd_4		
ePf_4, eNf_4	(0.0, 1.0) $\rtimes$ $Para_{RL}$	The values of these parameters are generally smaller than corresponding values describing the last key point.
$gK_1, gK_2, gK_3, gK_4, gK_{lim}$		
$gD_1, gD_2, gD_3, gD_4, gD_{lim}$		
$gF_1, gF_2, gF_3, gF_4, gF_{lim}$	min (1.0, (0.0, 5.0) $\rtimes$ $Para_R$)	The values of these parameters lie in (0.0, 1.0).
$rDispP, rDispN$		
$fForceP, fForceN$		
$uForceP, uForceN$		
gE, Gap_1, Gap_2	(0.0, 5.0) $\rtimes$ $Para_R$	-

better optimal solution but increases the difficulty in getting such solutions, thus may lead to a worse final solution. Therefore, after taking all the aforementioned factors into consideration and referring to existing studies[47, 30, 42, 6], the parameters are reversely normalized to the ranges shown in Table 4. The definitions of these parameters are provided in Appendix A.

In Table 4, $Para_R$ represents the value of corresponding reference parameter, and $Para_{RL}$ represents the corresponding parameter describing the last key point in the backbone curve. All the $Para_R$ and $Para_{RL}$ are obtained in Section 5.3. For example, for the parameter ePd_3, the $Para_R$ and $Para_{RL}$ refer to the values of ePd_3 and ePd_2 obtained in Section 5.3, respectively. It should be noted that, the ranges listed in Table 4 is not the optimal solution. There definitely exists some other ranges that lead to a more accurate parameter identification results or a more efficient optimization process. However, finding the optimal solution is quite time-consuming, and is not the main focus of the current study. Therefore, on condition that the ranges listed in Table 4 is verified in the following sections, the authors will not pay more attention on finely adjusting the searching ranges.

6.1.3. Preliminary parameter identification based on neural network

After the reverse normalization, all the sampled parameter combinations can be regarded as the input of the proposed joint-level OpenSeesPy model, and the simulations can be carried out to build the basic dataset for the neural network. Then, with the force response time-series as the input and the target parameter combination as the output, the neural network can be trained and verified. Some key settings of the neural network are listed in Table 5.

Table 5: Key settings of the neural network

Item	Setting
Dataset	10,000 samples (7:2:1 for training, validation and testing datasets, respectively)
Network architecture	Transformer with shortcuts [48, 49]
Input	Force time-series (with a sequence length of around 1,000)
Output	Parameters (40 dimensional vector)
Loss function	Mean square error (MSE)
Training device	RTX 4090 GPU

6.1.4. GA optimization on joint and roof truss scales

Based on the PGA algorithm introduced in Section 5.3, further optimizations will be carried out on joint and roof truss scales consequently. During the first PGA optimization process on the joint scale, the parameters obtained through neural network inference are adopted as the initial population. After that, the best solutions obtained in the first PGA optimization stage (joint scale) are selected as the initial population of the second PGA optimization stage (roof truss scale). The significant computational burden of roof truss models is the main reason that hinders the directly adopting of PGA optimization on roof truss scale (Step 5). Noting that, for contrast, the direct PGA optimization on both the joint and roof truss scales are also carried out in this study.

6.2. Results and discussions

6.2.1. Neural network prediction results

The neural networks established before are submitted for training multiple times, and the hyperparameters are tuned based on the validation losses. During the dataset generation process, compared to direct sampling methods, the proportion of divergent samples significantly decreases in simulations conducted with parameter combinations sampled from a uniform distribution and refined through reverse normalization guided by prior knowledge. This reduction can serve as indirect evidence of the effectiveness of this approach.

Among all the final inference results, the distribution of MSE values (Figure 16a), together with three typical samples with the minimum MSE (26.40, Figure 16b), average MSE (149.96, Figure16c) and maximum MSE (402.69, Figure16d), are presented here. It can be seen that the neural network prediction results are not very accurate, yet is qualified as a preliminary identification, because the predicted results reflect the overall response characteristics of the target joints. At this stage, the accuracy benefits of reverse normalization guided by prior knowledge are not immediately apparent and will be discussed later.

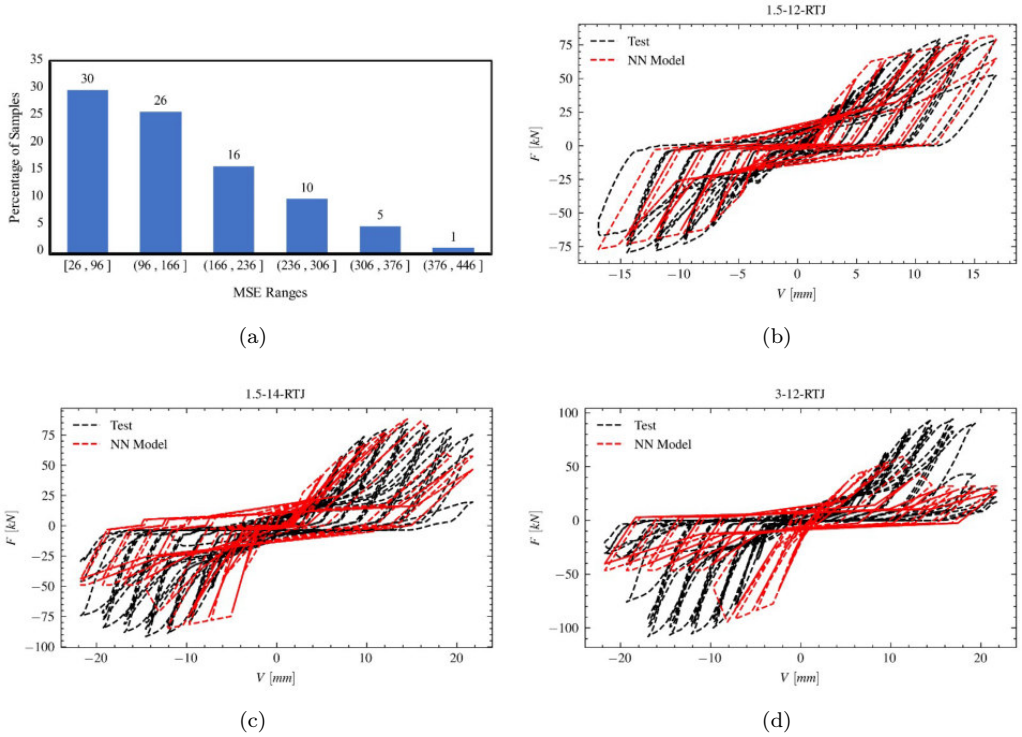

Figure 16: MSE distributions of neural network prediction results (a) and typical samples with minimum MSE (b), average MSE (c) and maximum MSE (d)

6.2.2. GA optimization results on joint scale

The GA optimization results on joint scale are shown in Figure 17. The information for all the labels and corresponding results are presented in Table 6. According to Figure 17 and Table 6, the following conclusions can be drawn:

Table 6: Information of labels and corresponding results on joint scale

Model type	Initial population	Searching space	Minimum MSE in each case			
			1.5-12-RTJ	3-12-RTJ	1.5-14-RTJ	3-14-RTJ
GA-V1	Randomly generated	Prior knowledge guided (Table 4)	8.34	20.42	20.78	23.47
GA-V2	Randomly generated	0.2-5 times of parameters in Section 5.3	15.94	38.39	29.74	40.65
GA-V3	From neural network	Prior knowledge guided (Table 4)	6.97	15.51	18.48	17.86
Neural network only	-	-	26.4	99.25	72.22	86.5
Parameters in Section 5.3	-	-	42.42	45.53	20.20	48.47

(1) The prior knowledge guided searching space provided in Table 4 results in a very significant accuracy improvement (MSE reduction). Compared with the group with random searching space (GA-V2), the optimization results are much better in GA-V1 (41.7% MSE reduction on average).

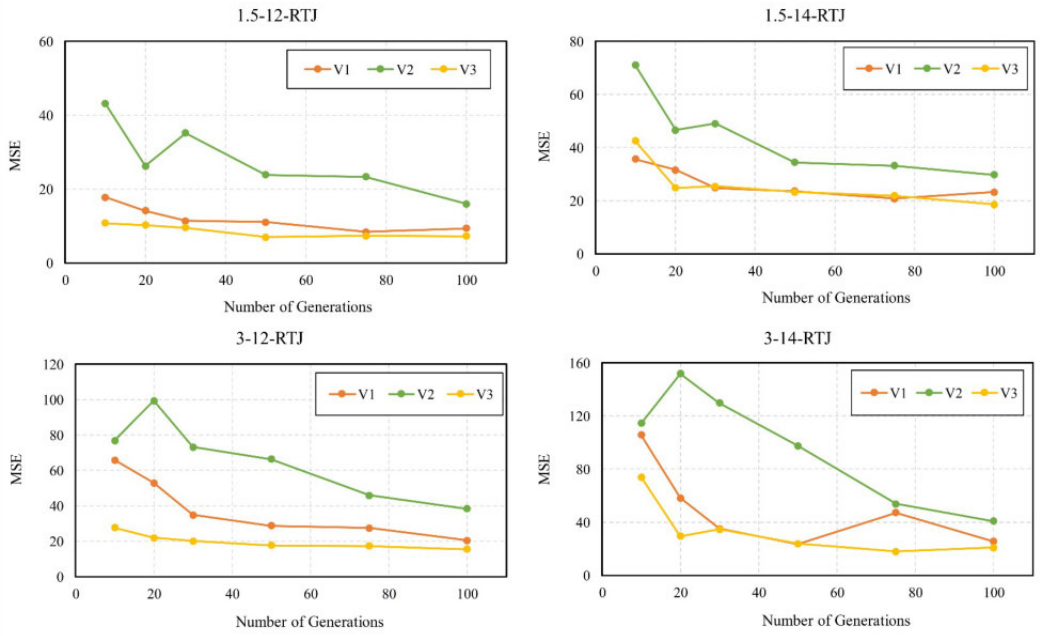

Figure 17: GA optimization results on joint scale

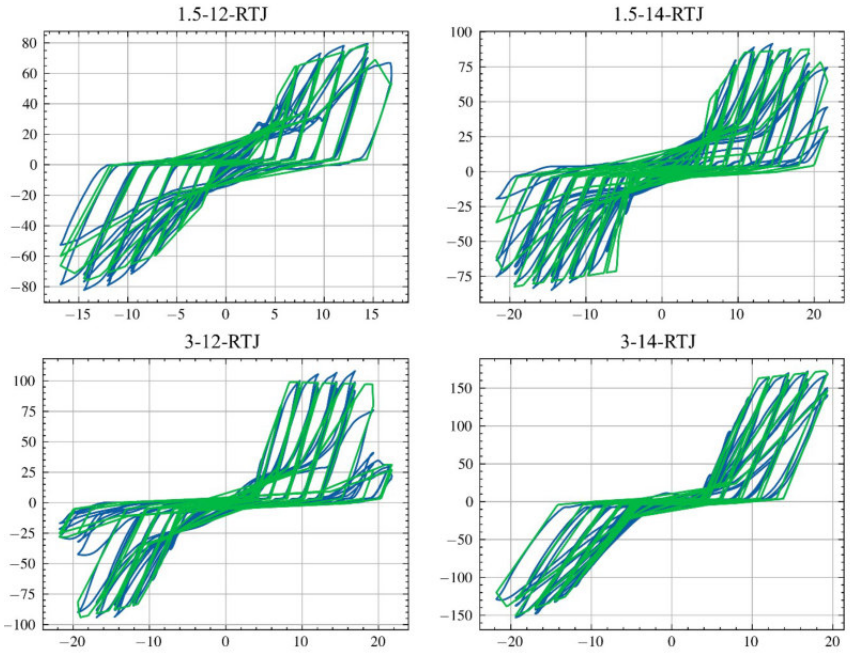

Figure 18: The optimal response behaviors on joint scale (blue curve: experimental results; green curve: the optimal simulation results)

(2) Although the preliminary identification of the neural network is not very accurate, the GA-V3 supported by neural network draws the best performance on all the joint cases, which proves the effectiveness

of the proposed framework on joint level. Compared with GA-V1 and results in Section 5.3, the average MSE reduction ratios are 18.9% and 55.3%, respectively.

The optimal simulated response behaviors for all four joint cases are shown in Figure 18, and corresponding parameters are listed in Appendix C.

6.2.3. GA optimization results on roof truss scale

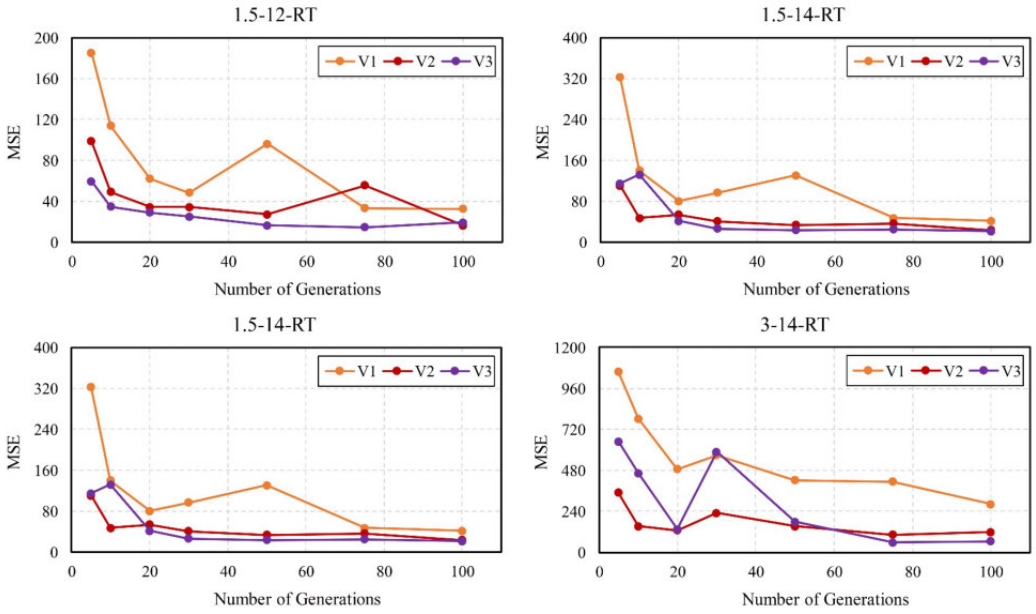

Figure 19: GA optimization results on roof truss scale

The GA optimization results on roof truss scale are shown in Figure 19. The information for all the labels and corresponding results are presented in Table 7. According to Figure 19 and Table 7, the following conclusions can be drawn:

Table 7: Information of labels and corresponding results on roof truss scale

Model type	Initial population	Searching space	Minimum MSE in each case			
			1.5-12-RT	3-12-RT	1.5-14-RT	3-14-RT
GA-V1-RT	Randomly generated	0.2-5 times of parameters in Section 5.3	32.57	94.11	41.61	282.37
GA-V2-RT	Randomly generated	Prior knowledge guided (Table 4)	16.47	31.37	23.16	102.2
GA-V3-RT	From GA optimization on joint scale (Section 6.2.2)	Prior knowledge guided (Table 4)	14.47	35.56	20.97	57.81

(1) The effectiveness of the prior knowledge guided searching space is further verified based on the comparison between GA-V1-RT and GA-V2-RT, within which significant MSE reduction (56.1% on average) can be observed for all cases.

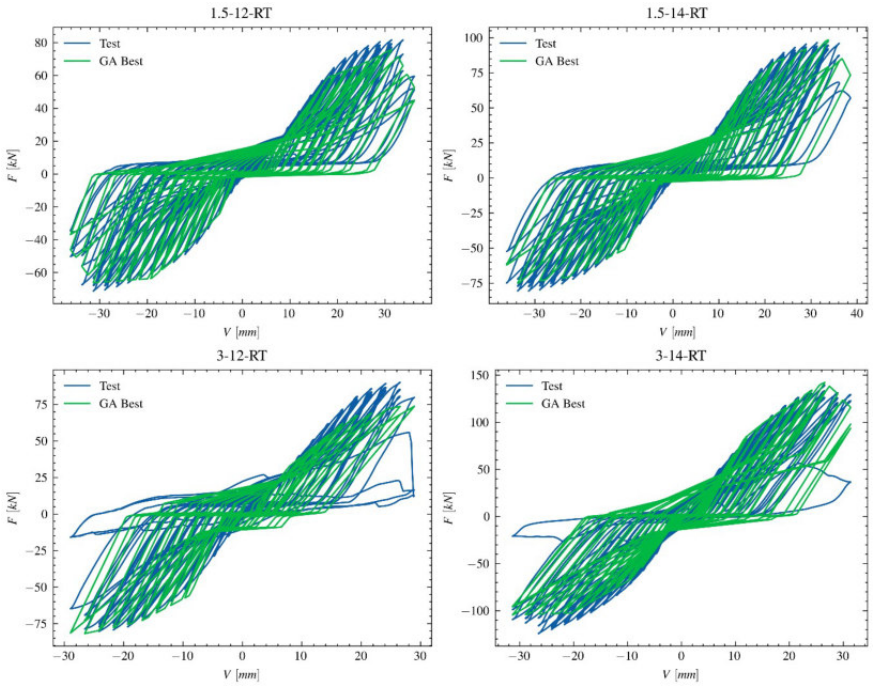

Figure 20: Best simulated response behaviors on roof truss scale (blue curve: experimental results; green curve: the optimal simulation results)

(2) The optimization based on the initial population from GA optimization on joint scale (group GA-V3-RT in Table 7) reaches the best performance in most cases, except for a slightly worse result in case 3-12-RT. Compared with the group that directly carrying out the GA optimization (group GA-V2-RT), the average MSE reduction ratio for four roof truss cases is 12.9%.

The best solutions for all four roof truss cases are shown in Figure 20, and corresponding parameters are listed in Appendix C.

7. Verification of global truss model

In Section 6, four roof truss models were updated based on the proposed model updating workflow. In this section, the updated models are further validated against the mid-span deflection time series for node 2 and measured strain time series for each chord. The finally updated model parameters listed in Appendix C were used as input for the proposed roof truss model.

7.1. Comparison of mid-span deflection over time at node 2

The result of mid-span deflection over time at node 2 measured by the LVDT is shown in Figure 21. The obtained results are then compared with the corresponding numerical simulation results. Generally,

Table 8: *RRMSE* between the tested and predicted responses (deflection at Node 2)

	Deflection at Node 2			
Configuration	1.5-12-RT	3-12-RT	1.5-14-RT	3-14-RT
RRMSE	14.32%	12.45%	12.68%	8.75%

the numerical results provide a good agreement with test results. To quantitatively compare the prediction accuracy, the Relative Root Mean Square Errors (RRMSE) are calculated, as shown in Table 8, which provides a measurement of the relative error between the tested and simulated responses. Using RRMSE as the error index, the prediction error of deflection at Node 2 is controlled within 15% for all types of roof trusses.

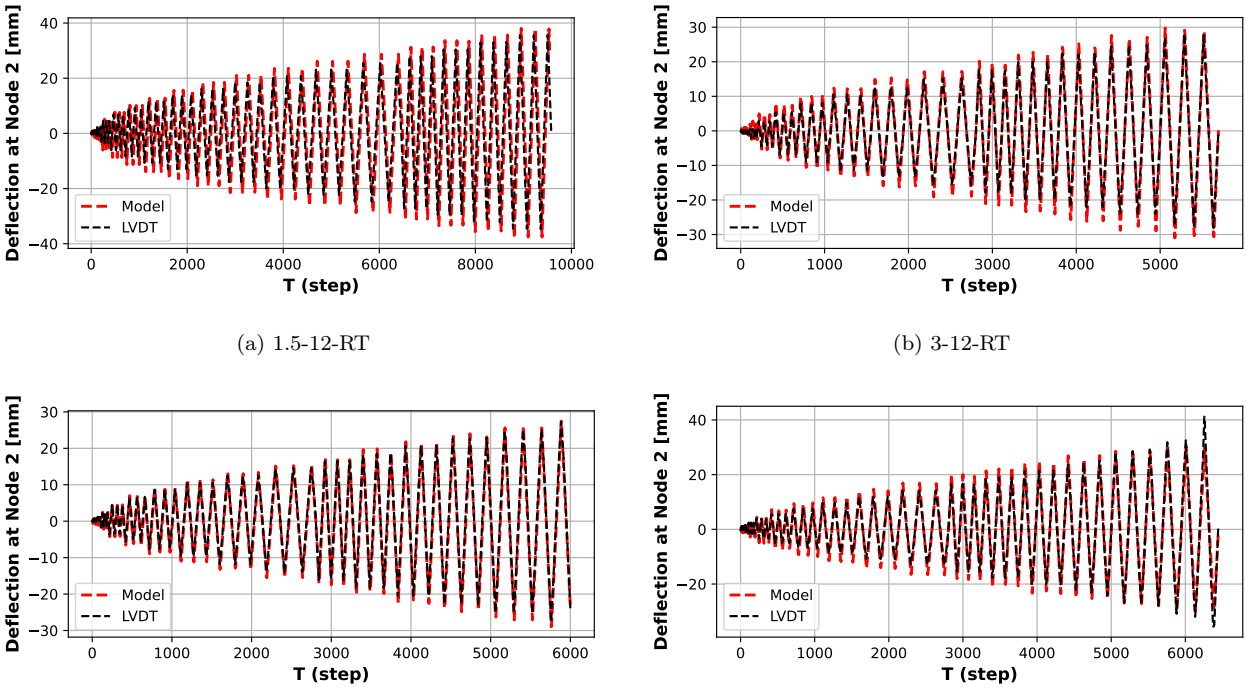

(a) 1.5-12-RT

(b) 3-12-RT

(c) 1.5-14-RT

(d) 3-14-RT

Figure 21: Comparison of mid-span deflection over time at node 2 obtained from the numerical simulation (label "model") and test (label "LVDT").

7.2. Comparison of strain curves for each chord

As an illustrative example, Figure 22 showcases the strain curves over time for each chord of glubam roof truss, as accurately measured by the strain gauge. The obtained strain curves are then compared with the corresponding numerical simulation results, providing a comprehensive assessment of their agreement. Generally, the absolute strain value errors can be controlled within 0.0002. Table 9 quantitatively compares

Table 9: *RRMSE* between the tested and predicted responses regarding to strain values at each chord (3,4,5,8).

	Strain value at each chord (3,4,5,8)			
Configuration	Chord 3	Chord 4	Chord 5	Chord 8
1.5-12-RT	21.32%	18.45%	19.68%	18.75%
3-12-RT	9.15%	16.32%	11.42%	15.21%
1.5-14-RT	8.32%	15.68%	18.31%	16.56%
3-14-RT	8.65%	8.72%	6.53%	12.32%

the prediction accuracy using RRMSE as the error index. Generally, the prediction error in terms of strain value at each chord can be controlled within 25% for all types of roof trusses when using RRMSE as the error index. Additionally, the internal force of truss chord 3 is the largest, indicating that the failure usually originated from this chord, which is consistent with the experimental observation. Therefore, the accuracy of the proposed model and updated parameters are verified.

8. Conclusions and Discussions

8.1. Conclusions

This study conducted a thorough investigation of the hysteretic behaviors of riveted glubam connections integrated with thin-walled steel tubes and their corresponding roof trusses. Experiments on joints and roof trusses, spanning four distinct configurations, were executed. A preliminary parameter identification method, PGA, along with a more sophisticated model updating framework, were both developed and validated. The key findings are as follows:

(1) The experimental outcomes for both joints and roof trusses demonstrated that well-designed joints exhibit ductile behavior. Such joints contribute significantly to enhancing seismic resilience in glubam structures.

(2) With appropriate parameters, a OpenSeesPy model is proposed by combining the Pinching4 and IEPPG elements, which can accurately and efficiently capture the hysteretic characteristics of both the joints and roof trusses. These models can simulate the hysteretic behaviors across various stages, including initial slip, elastic phase, yielding phase, loading plateau, and failure.

(3) The innovative model updating approach, combining neural networks, searching space guided by prior knowledge, and PGA, provides a robust technique for parameter identification in highly non-linear and non-convex contexts with both precision and speed.

8.2. Discussions

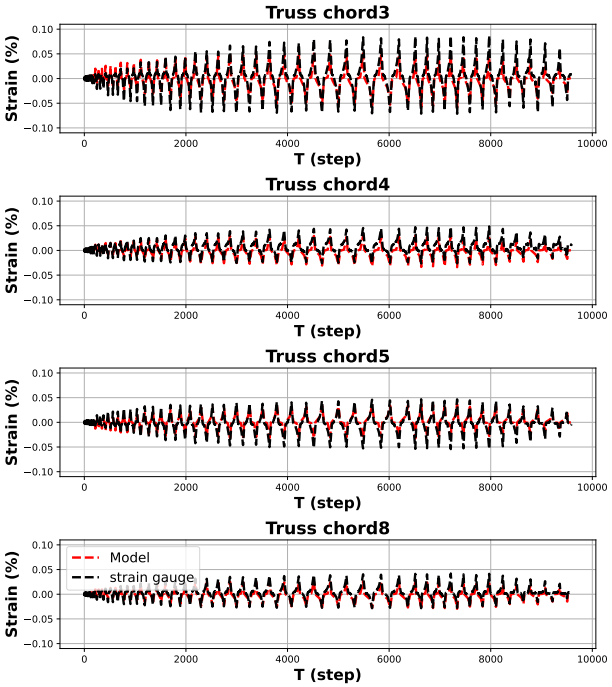

(a) 1.5-12-RT

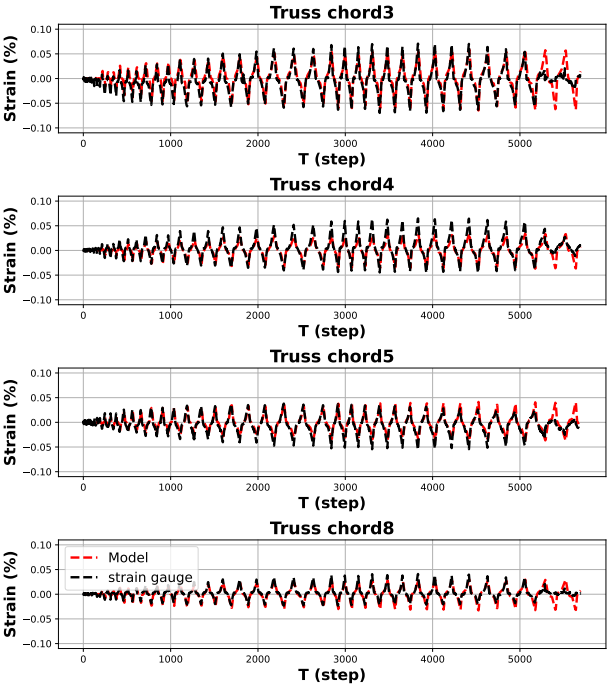

(b) 3-12-RT

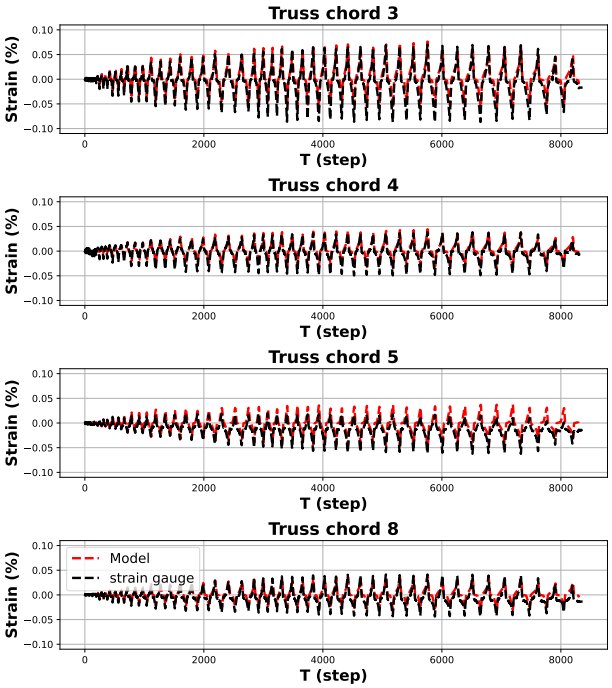

(c) 1.5-14-RT

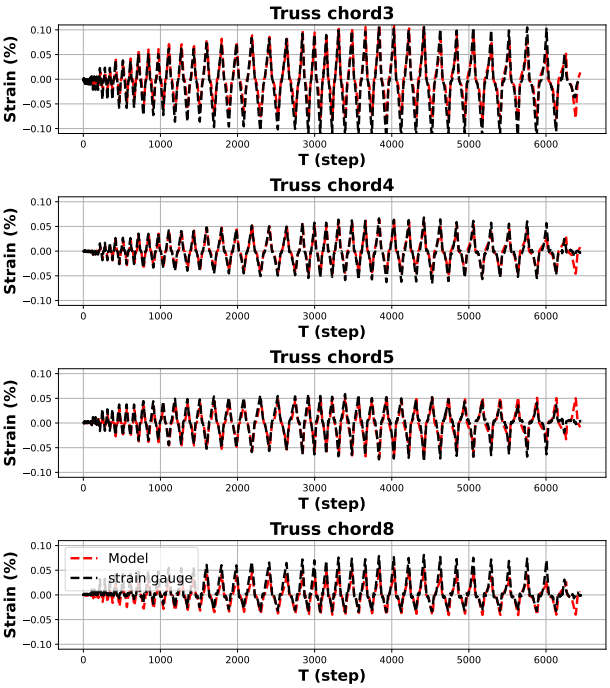

(d) 3-14-RT

Figure 22: Comparison of strain curves obtained from the numerical simulation and test for chords 3,4, 5 and 8

The research process has also identified several limitations in the use of glubam for roof trusses, primarily related to material variability, connection assembly, and model limitations. Like all natural materials, glubam exhibits inherent variability in its properties, which can influence its performance and reliability in structural applications. Understanding and managing the material variability of glubam is critical for its reliable use in construction. Engineers and architects must account for this variability in their designs to ensure safety and performance. This may involve using conservative design values, implementing extensive testing protocols, and adopting advanced modeling techniques to predict the behavior of glubam structures under various conditions. In addition, information about the long-term durability and performance of glubam and steel tube connections under various environmental conditions would enhance the practical relevance of the findings. Furthermore, the connection assembly of glubam roof trusses poses several difficulties. While riveted steel tube joints offer advantages in terms of strength and durability, they also introduce challenges such as precise alignment and secure fastening. Improper assembly can lead to stress concentrations and potential failure in the structure. Additionally, due to the proposed model having nearly 40 parameters, if the initial parameters are not chosen well, there may be convergence and stability issues during the optimization process using the PGA. In summary, addressing these issues requires a multidisciplinary approach, combining advances in material science, structural engineering, and computational modeling.

Based on the current findings about the glubam roof truss with riveted hollow steel tube joints, several areas merit further exploration to advance the understanding and application of this innovative construction material. Outlined below are specific future research directions that could provide valuable insights and improvements:

(1) Investigate the long-term mechanical behaviors and durability of bio-based materials. This is important for the practical application of the bio-based materials in real-world situations.

(2) Investigate the performance of other bio-based materials, such as laminated veneer lumber (LVL) or cross-laminated timber (CLT), in combination with hollow steel tube joints, which provides a comparative analysis supporting the identification of materials with superior properties for specific applications.

(3) Develop hybrid construction systems that integrate glubam with other sustainable materials, examining the synergistic effects on structural performance, durability, and sustainability.

(4) Develop new connection techniques that enhance the performance of glubam roof trusses. This includes the design of more efficient rivet patterns, the use of adhesive bonding in conjunction with mechanical fasteners, and the exploration of alternative fastening methods like self-tapping screws or bolts.

(5) Incorporate smart materials and sensors into the connections to monitor structural health in real-time, enabling proactive maintenance and enhancing the longevity of the structures.

Acknowledgments

This research is supported by the National Key Research and Development Program of China (2019YFD1101002), the Zhejiang University - University of Illinois Urbana-Champaign Institute and the Chaoyong project from Haining municipal government.

Declaration of Competing Interest

The authors declare that they have no known competing financial interests or personal relationships that could have appeared to influence the work reported in this paper.

Data availability

The data that support the findings of this study are available from the corresponding author upon reasonable request.

References

[1] S. R. Imadi, I. Mahmood, A. G. Kazi, Bamboo fiber processing, properties, and applications, 2014. URL: https://api.semanticscholar.org/CorpusID:135557420.

[2] Y. Xiao, Z. Li, K. Liu, Modern engineered bamboo structures, 2019.

[3] K. Chung, W. Yu, Mechanical properties of structural bamboo for bamboo scaffoldings, Engineering Structures 24 (2002) 429–442.

[4] L. Villegas, R. Morán, J. J. García, A new joint to assemble light structures of bamboo slats, Construction and Building Materials 98 (2015) 61–68.

[5] Y. Xiao, R. Yang, B. Shan, Production, environmental impact and mechanical properties of glubam, Construction and Building Materials 44 (2013) 765–773.

[6] D. Shi, Y. Xu, C. Demartino, Y. Xiao, B. F. Spencer, Bio-based laminated truss structures with bolted steel connections: Experiment, modeling, and model-updating, Earthquake Engineering & Structural Dynamics 53 (2024) 739–755.

[7] B. Sharma, A. Gatóo, M. Bock, M. Ramage, Engineered bamboo for structural applications, Construction and Building Materials 81 (2015) 66–73.

[8] H. Li, Z. Li, Prefabricated bamboo-steel hybrid structures: Design and construction, Advanced Materials Research 1130 (2017) 242–247.

[9] M. Chen, L. Ye, H. Li, G. Wang, Q. Chen, C. Fang, C. Dai, B. Fei, Flexural strength and ductility of moso bamboo, Construction and Building Materials 246 (2020) 118418.

[10] M. Popovski, E. Karacabeyli, Seismic behaviour of structural systems with riveted connections in timber construction 7 (2006) 4143–4152.

[11] Z. Chen, M. Popovski, Seismic response of braced heavy timber frames with riveted connections, Journal of Performance of Constructed Facilities 35 (2021). doi:10.1061/(ASCE)CF.1943-5509.0001618.

[12] Q. Zhou, J. Zhu, Study on the mechanical performance of bamboo-steel composite beams, Journal of Building Engineering 18 (2018) 409–418.

[13] B. Murty, A. Asiz, I. Smith, Tests and models for engineered wood product connections using small steel tube fasteners, Engineering Structures 33 (2011) 63–68.

[14] J. J. A. Janssen, Designing and Building with Bamboo, Technical Report, International Network for Bamboo and Rattan, 2000.

[15] N. Nugroho, N. Ando, Development of structural composite products made from bamboo i: Fundamental properties of bamboo zephyr board, Journal of Wood Science 46 (2012) 68–74.

[16] A. Citipitioglu, R. Haj-Ali, D. White, Refined 3d finite element modeling of partially-restrained connections including slip, Journal of constructional Steel research 58 (2002) 995–1013.

[17] M. Izzi, A. Polastri, M. Fragiacomo, Modelling the mechanical behaviour of typical wall-to-floor connection systems for cross-laminated timber structures, Engineering Structures 162 (2018) 270–282.

[18] F. Wang, J. Yang, Experimental and numerical investigations on load-carrying capacity of dowel-type bolted bamboo joints, Engineering Structures 209 (2020) 109952.

[19] C. Kim, K. M. Min, H. Choi, H. J. Kim, M.-G. Lee, Development of analytical strength estimator for self-piercing rivet joints through observation of finite element simulations, International Journal of Mechanical Sciences 202 (2021) 106499.

[20] J. Zhao, Y. Peng, W. Su, J. Dong, Finite element analysis of the shear capacity of stainless-steel blind-rivet connections, Journal of Constructional Steel Research 179 (2021) 106558.

[21] L. W. Ehrlich, A modified newton method for polynomials, Communications of the ACM 10 (1967) 107–108.

[22] J. E. Dennis, Jr, J. J. More, Quasi-newton methods, motivation and theory, SIAM review 19 (1977) 46–89.

[23] R. Astroza, H. Ebrahimian, J. P. Conte, Material parameter identification in distributed plasticity fe models of frame-type structures using nonlinear stochastic filtering, Journal of Engineering Mechanics 141 (2015) 04014149.

[24] Z. Yu, L. Xiao, H. Li, X. Zhu, R. Huai, Model parameter identification for lithium batteries using the coevolutionary particle swarm optimization method, IEEE Transactions on Industrial Electronics 64 (2017) 5690–5700.

[25] H. Ebrahimian, R. Astroza, J. P. Conte, R. A. de Callafon, Nonlinear finite element model updating for damage identification of civil structures using batch bayesian estimation, Mechanical Systems and Signal Processing 84 (2017) 194–222.

[26] R. Astroza, A. Alessandri, J. P. Conte, A dual adaptive filtering approach for nonlinear finite element model updating accounting for modeling uncertainty, Mechanical Systems and Signal Processing 115 (2019) 782–800.

[27] S. Sessa, N. Vaiana, M. Paradiso, L. Rosati, An inverse identification strategy for the mechanical parameters of a phenomenological hysteretic constitutive model, Mechanical Systems and Signal Processing 139 (2020) 106622.

[28] T. Wang, M. Noori, W. A. Altabey, M. Farrokh, R. Ghiasi, Parameter identification and dynamic response analysis of a modified prandtl–ishlinskii asymmetric hysteresis model via least-mean square algorithm and particle swarm optimization, Proceedings of the Institution of Mechanical Engineers, Part L: Journal of Materials: Design and Applications 235 (2021) 2639–2653.

[29] B. Do, M. Ohsaki, Bayesian optimization for inverse identification of cyclic constitutive law of structural steels from cyclic structural tests, in: Structures, volume 38, Elsevier, 2022, pp. 1079–1097.

[30] Y. Gu, X. Lu, Y. Xu, A deep ensemble learning-driven method for the intelligent construction of structural hysteresis models, Computers & Structures 286 (2023) 107106.

[31] M. Zhu, F. McKenna, M. H. Scott, Openseespy: Python library for the opensees finite element framework, SoftwareX 7 (2018) 6–11.

[32] T. Vallee, T. Tannert, S. Hehl, Experimental and numerical investigations on full-scale adhesively bonded timber trusses, Materials and Structures 44 (2011) 1745–1758.

[33] Y. Xiao, G. Chen, L. Feng, Experimental studies on roof trusses made of glubam, Materials and Structures 47 (2013) 1879–1890.

[34] S. Silih, M. Premrov, S. Kravanja, Optimum design of plane timber trusses considering joint flexibility, Engineering

Structures 27 (2005) 145–154.

[35] GB50005, Code for design of timber structures, 2017.

[36] G. Winiarski, T. Bulzak, Wójcik, M. Szala, Effect of tool kinematics on tube flanging by extrusion with a moving sleeve, Advances in Science and Technology Research Journal 13 (2019) 210–216.

[37] E. C. for Standardization (CEN), Timber structures-test methods-cyclic testing of joints made with mechanical fasteners, European Standard. 2001;12512 (2001).

[38] J. Cao, H. Xiong, J. Wang, J. Kang, Model updating for timber-framed construction using the full-scale test, Engineering Structures 213 (2020) 110560.

[39] J. Cao, H. Xiong, Y. Liu, Experimental study and analytical model of bolted connections under monotonic loading, Construction and Building Materials 270 (2021) 121380.

[40] V. Skorpil, V. Oujezsky, P. Cika, M. Tuleja, Parallel processing of genetic algorithms in python language, in: 2019 PhotonIcs and Electromagnetics Research Symposium, 2019, pp. 3727–3731.

[41] O. Hasançebi, T. Bahçecioğlu, Kurç, M. Saka, Optimum design of high-rise steel buildings using an evolution strategy integrated parallel algorithm, Computers Structures 89 (2011) 2037–2051.

[42] D. Shi, G. C. Marano, C. Demartino, Bio-based connections and hybrid planar truss: A parallel genetic algorithm approach for model updating, Computers & Structures 301 (2024) 107463.

[43] G. Di Gangi, C. Demartino, G. Quaranta, G. Monti, Dissipation in sheathing-to-framing connections of light-frame timber shear walls under seismic loads, Engineering Structures 208 (2020) 110246.

[44] W.-L. Loh, On latin hypercube sampling, The annals of statistics 24 (1996) 2058–2080.

[45] G. Sun, L. Li, J. Fang, Q. Li, On lower confidence bound improvement matrix-based approaches for multiobjective bayesian optimization and its applications to thin-walled structures, Thin-Walled Structures 161 (2021) 107248.

[46] Z. Kala, Sensitivity of load-carrying capacity of a thin-walled steel member to the initial curvature shape of its axis, in: Thin-Walled Structures, CRC Press, 2018, pp. 835–842.

[47] Y. Xu, Y. Fei, Y. Huang, Y. Tian, X. Lu, Advanced corrective training strategy for surrogating complex hysteretic behavior, in: Structures, volume 41, Elsevier, 2022, pp. 1792–1803.

[48] A. Vaswani, N. Shazeer, N. Parmar, J. Uszkoreit, L. Jones, A. N. Gomez, L. Kaiser, I. Polosukhin, Attention is all you need, Advances in neural information processing systems 30 (2017).

[49] Y. Xu, X. Lu, Y. Fei, Y. Huang, Hysteretic behavior simulation based on pyramid neural network: Principle, network architecture, case study and explanation, Advances in Structural Engineering (2023) 13694332231184322.

Appendix A. Material constitutive law in empirical model

Table A.10: Parameters of the Pinching4 material in OpenSeesPy [31].

Parameters	Description
$ePf_1, ePf_2, ePf_3, ePf_4, ePd_1, ePd_2, ePd_3, ePd_4$	denotes the force and deformation points on the positive response envelope
$eNf_1, eNf_2, eNf_3, eNf_4, eNd_1; eNd_2; eNd_3; eNd_4$	denotes the force and deformation points on the negative response envelope
$gK_1, gK_2, gK_3, gK_4, gK_{lim}$	controls cyclic degradation model for unloading stiffness degradation
$gD_1, gD_2, gD_3, gD_4, gD_{lim}$	controls cyclic degradation model for reloading stiffness degradation
$gF_1, gF_2, gF_3, gF_4, gF_{lim}$	controls cyclic degradation model for strength degradation
$rDispP, rDispN$	denotes the ratio of the deformation at which reloading occurs to the max/min historic deformation demand
$fForceP, fForceN$	denotes the ratio of the force at which reloading begins to force corresponding to the max/min historic deformation demand
$uForceP, uForceN$	denotes the ratio of strength developed upon unloading from negative load to the max/min strength developed under monotonic loading
gE	denotes maximum energy dissipation

Table A.11: Parameters of the IEPPG material in OpenSeesPy [31].

Parameters	Description
E	tangent
Fy	stress or force at which material reaches plastic state
gap	initial gap
eta	hardening ratio (Eh/E)
$damage$	an optional string to specify whether to accumulate damage or not in the material

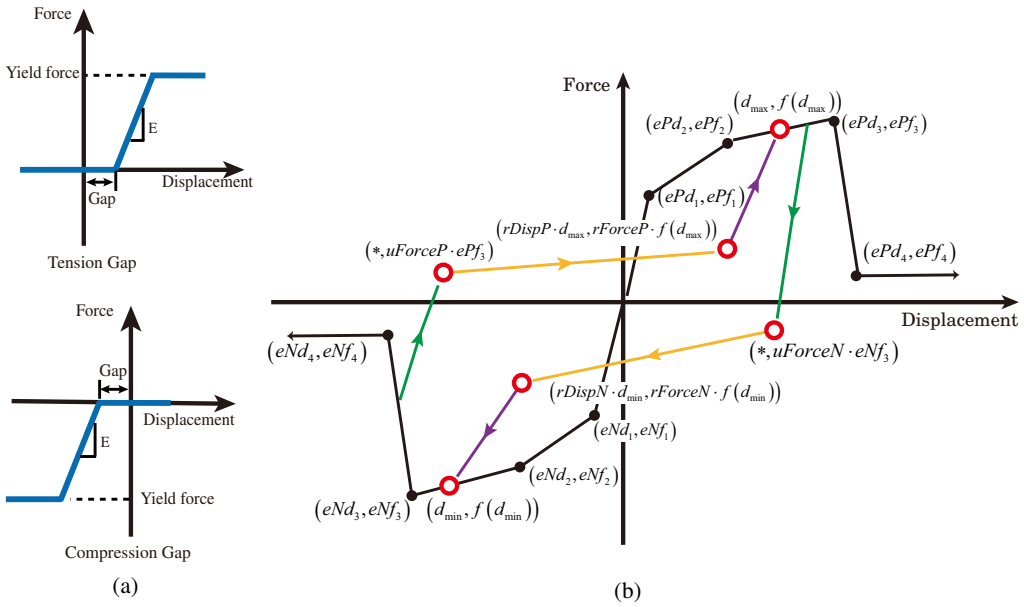

Figure A.23: Elastic-Plastic Gap (a) and Pinching4 Material (b) model. [38, 39]

Appendix B. Optimal parameters for all cases

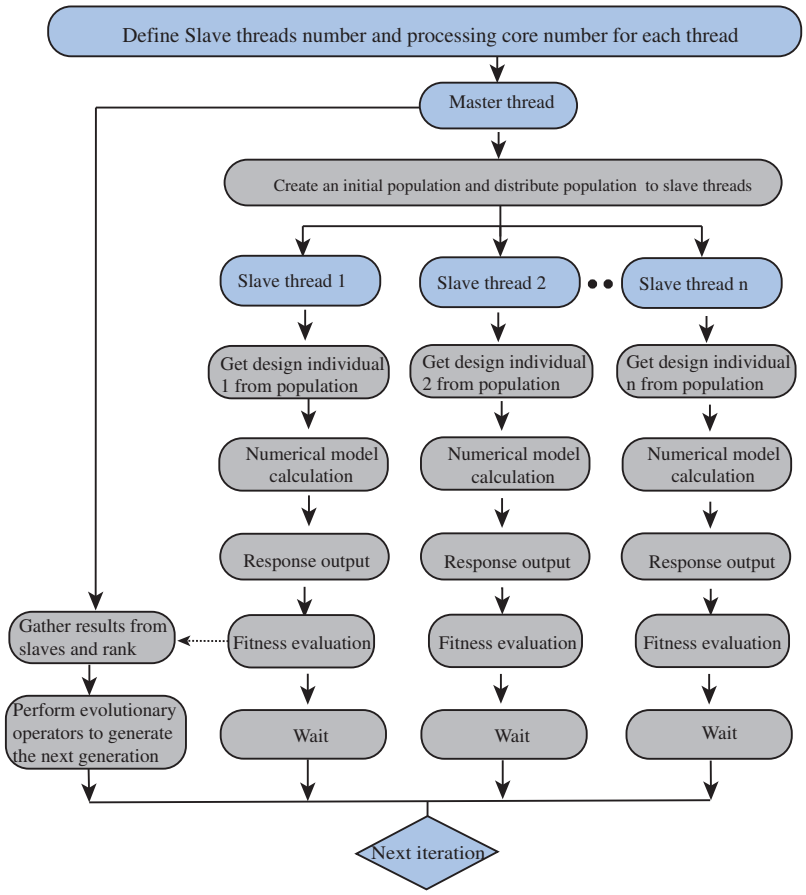

Figure B.24: Flowchart for parallel algorithm (modified based on [42])

Appendix C. Optimal parameters for all cases

Table C.12: Optimal parameters for all cases

Specimen	1.5-12-RTJ	3-12-RTJ	1.5-14-RTJ	3-14-RTJ	1.5-12-RT	3-12-RT	1.5-14-RT	3-14-RT
ePf_1	48.85	46.16	53.14	50.10	54.75	28.99	49.39	71.47
ePd_1	1.58	1.60	2.37	1.72	1.91	0.61	0.92	0.63
ePf_2	73.83	116.05	86.14	174.63	61.98	64.41	77.36	123.22
ePd_2	3.55	4.99	7.42	7.02	3.68	2.92	2.85	3.32
ePf_3	89.99	113.80	86.59	185.12	71.42	100.34	94.43	125.47
ePd_3	10.83	15.92	17.00	15.23	5.63	14.09	5.92	3.53
ePf_4	61.02	36.53	36.28	157.91	28.92	36.42	63.36	83.31
ePd_4	13.21	16.18	20.10	17.90	9.85	14.99	8.39	7.43
eNf_1	-30.60	-57.44	-14.49	-35.43	-22.55	-53.68	-47.24	-55.83
eNd_1	-1.63	-3.06	-0.90	-2.09	-0.34	-0.39	-0.90	-0.92
eNf_2	-68.04	-97.62	-69.52	-134.84	-59.99	-71.73	-67.09	-90.19
eNd_2	-6.37	-6.23	-5.65	-9.10	-3.23	-2.51	-4.42	-3.62
eNf_3	-86.98	-110.63	-86.63	-162.16	-62.43	-111.78	-71.98	-99.30
eNd_3	-13.33	-13.86	-17.91	-15.49	-6.89	-16.14	-8.44	-21.94
eNf_4	-73.59	-33.19	-37.51	-88.38	-27.47	-101.60	-38.22	-93.04
eNd_4	-16.69	-15.05	-21.79	-20.21	-10.81	-17.13	-12.32	-36.25
$rDispP$	0.47	0.51	0.53	0.25	0.41	0.20	0.47	0.96
$fForceP$	0.45	0.29	0.38	0.15	0.34	0.33	0.40	0.55
$uForceP$	0.01	0.00	0.00	0.00	0.06	0.07	0.05	0.04
$rDispN$	0.30	0.48	0.36	0.09	0.44	0.23	0.23	0.16
$fForceN$	0.30	0.39	0.21	0.16	0.05	0.15	0.05	0.16
$uForceN$	0.02	0.02	0.00	0.01	0.00	0.08	0.00	0.03
gK_1	0.35	0.26	0.28	0.19	0.04	0.21	0.42	0.53
gK_2	0.10	0.26	0.04	0.84	0.04	0.74	0.03	0.89
gK_3	1.00	0.67	0.92	0.84	0.96	0.41	0.95	0.83
gK_4	0.23	0.24	0.24	0.03	0.24	0.15	0.18	0.18
gK_{lim}	0.37	0.80	0.56	0.10	0.41	0.55	0.28	0.38
gD_1	0.65	0.01	0.25	0.03	0.04	0.31	0.48	0.49
gD_2	0.45	0.19	0.27	0.05	0.06	0.46	0.19	0.07
gD_3	0.99	0.97	0.22	0.04	0.24	0.34	0.36	1.00
gD_4	0.19	0.25	0.20	0.21	0.23	0.15	0.20	0.23
gD_{lim}	0.07	0.21	0.11	0.16	0.09	0.19	0.22	0.20
$gF1$	0.85	0.87	0.76	0.84	0.86	0.07	0.31	0.59
$gF2$	0.44	0.02	0.33	0.62	0.56	0.50	0.69	0.09
$gF3$	0.10	0.09	0.17	0.04	0.09	0.14	0.13	0.19
$gF4$	0.19	0.23	0.21	0.05	0.17	0.05	0.01	0.16
$gFLim$	0.13	0.15	0.00	0.07	0.16	0.18	0.16	0.10
gE	72.38	81.78	58.28	4.70	69.56	38.54	63.92	71.44
Gap_1	-0.74	-5.27	-2.48	-4.14	-0.11	-0.39	-0.16	-0.00
Gap_2	3.51	3.36	3.60	3.78	0.52	0.32	0.54	0.54